PNAS RESEARCH ARTICLE | APPLIED PHYSICAL SCIENCES

Probing active nematics with in situ microfabricated elastic inclusions

Ignasi Vélez-Cerón[a,b], Pau Guillamat[c], Francesc Sagués[a,b], and Jordi Ignés-Mullol[a,b,1]

Edited by Luca Giomi, Universiteit Leiden, Leiden, Netherlands; received July 24, 2023; accepted January 27, 2024 by Editorial Board Member Mehran Kardar

In this work, we report a direct measurement of the forces exerted by a tubulin/kinesin active nematic gel as well as its complete rheological characterization, including the quantification of its shear viscosity, η, and its activity parameter, α. For this, we develop a method that allows us to rapidly photo-polymerize compliant elastic inclusions in the continuously remodeling active system. Moreover, we quantitatively settle long-standing theoretical predictions, such as a postulated relationship encoding the intrinsic time scale of the active nematic in terms of η and α. In parallel, we infer a value for the nematic elasticity constant, K, by combining our measurements with the theorized scaling of the active length scale. On top of the microrheology capabilities, we demonstrate strategies for defect encapsulation, quantification of defect mechanics, and defect interactions, enabled by the versatility of the microfabrication strategy that allows to combine elastic motifs of different shapes and stiffnesses that are fabricated in situ.

soft active matter | hydrogel | rheology | topological defects | micro fabrication

Significance

Synthetic active biomaterials are valuable tools to explore and understand the organization and dynamics of complex living systems. Proposed theories face limitations in their use since they are based on a few parameters that are challenging to measure. Our work introduces a microfabrication method for the in situ polymerization of hydrogel structures within an active nematic gel. This has allowed us to measure the forces exerted by this active material, its shear viscosity, activity parameter, and the bend rigidity. Our measurements also enable a quantitative mapping of the forces around topological defects, which not only play a fundamental role in biological organization but also hold the potential to drive advancements in biohybrid machines in the future.

Active matter embraces a wide variety of systems composed of dense collections of units that continuously convert energy into forces, thus being inherently out of equilibrium (1). Interactions between these force-generating units lead to collective phenomena such as flocking, seemingly turbulent flows, and other emergent mechanodynamical patterns (2, 3). Besides the many natural examples that can be found at different length scales (4–6), similar phenomena can be obtained in vitro by bottom–up approaches based on the densification of active colloidal particles including, for instance, monolayers of mammalian cells (7–10), self-propelled particles (11–14), living bacteria (15–18) or reconstitutions of cytoskeletal filaments and motor proteins (19, 20).

The latter systems are among the most fascinating examples in the field of synthetic active matter (21). At the expense of adenosine triphosphate (ATP) consumption, bound molecular motor clusters internally shear protein filament bundles, leading to continuous chaotic flows. In a dense, quasi-two-dimensional phase, known as active nematic (AN) (22, 23), these active gels feature continuously changing textures with liquid-crystal-like orientational (nematic) order. The latter is lost in local regions that configure topological defects.

Experiments have been able to characterize (24–26), even control (27, 28) and manipulate the dynamics of AN realizations (29–31), while theoretical and numerical works have successfully rationalized experimental observations (32–36). In spite of recent studies with monolayers of mammalian cells featuring nematic order (7, 37), little is known about the active mechanics of AN materials. More fundamentally, an accurate quantitative determination of the most important constitutive parameters of the microtubule-based AN system is lacking. Here, we address this challenge by embedding microfabricated elastic inclusions with pre-designed size and geometry within the AN layer. By studying the deformations of such objects we have been able to probe the system's rheology and mechanics.

Results and Discussion

In Situ Polymerization of Hydrogel Structures.

Modifications in the AN Formulation. We tune our active preparations by adding to the standard formulation of a kinesin/tubulin active gel the precursors of a hydrogel that can be photo-polymerized with UV light. This mixture is introduced in a flow cell with a gap of 50 microns between two glass plates (*Materials and Methods*, for full details). One plate incorporates a superhydrophilic polyacrylamide (PAM) brush, which prevents protein adsorption. The other plate is functionalized with fluorinated

Author contributions: P.G., F.S., and J.I.-M. designed research; I.V.-C. and J.I.-M. performed research; I.V.-C. contributed new reagents/analytic tools; I.V.-C. analyzed data; F.S. developed the theory; and I.V.-C., P.G., F.S., and J.I.-M. wrote the paper.

The authors declare no competing interest.

This article is a PNAS Direct Submission. L.G. is a guest editor invited by the Editorial Board.

[1] To whom correspondence may be addressed. Email: jignes@ub.edu.

This article contains supporting information online at https://www.pnas.org/lookup/suppl/doi:10.1073/pnas.2312494121/-/DCSupplemental.

Published March 7, 2024.

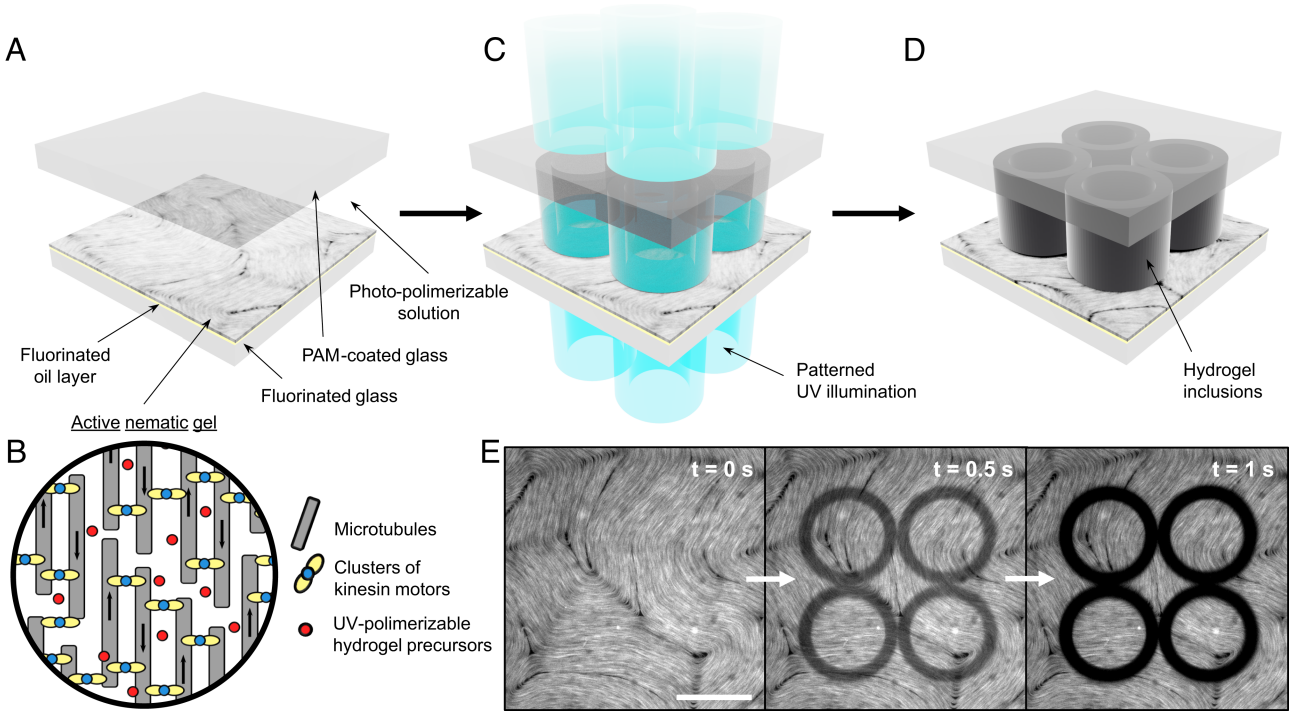

Fig. 1. In situ photo-polymerization of hydrogel structures in an active nematic (AN) gel. (*A*) Sketch of the experimental system. (*B*) Sketch of the microstructure within the AN filaments, where antiparallel microtubules slide due to the action of kinesin clusters. Arrows indicate the direction of microtubule motion. (*C* and *D*) Polymerization of four rigid hydrogel columnar rings (Movie S1). (*E*) Fluorescence micrographs before, during, and after UV illumination, and emergence of the hydrogel rings. The polymerized region is photobleached by the effect of UV light. Elapsed times are overlaid on each frame. (Scale bar, 50 μm.)

alkane chains that adsorb a thin layer of a fluorinated oil (Fig. 1 *A* and *B*). The active nematic forms at the water/oil interface, which is decorated with a polyethyleneglycol-based surfactant that prevents biomolecules from being in direct contact with the oil. As stated above, apart from the standard components of the active preparation, the aqueous subphase incorporates polyethyleneglycol-acrylate monomers and lithium phenyl-2,4,6-trimethylbenzoylphosphinate (LAP) (38), a photo-initiator molecule (Fig. 1*B* and Table 1). Irradiation with UV light induces the dissociation of LAP into radical species that initiate a chain polymerization reaction leading to the formation of a PEG hydrogel in the regions exposed to the UV light. In our experiments, we use a custom illumination setup based on a digital micromirror device (DMD) integrated into the light path of an inverted fluorescence microscope (*SI Appendix*, Fig. S1). Once the AN is formed, patterns of UV light are focused on the AN layer by means of the microscope objective, which sets the maximum size and lateral resolution of the built objects, as well as the range of power densities of the irradiation.

Hydrogel Structures with Arbitrary Stiffness. With this setup, we can generate in situ columnar hydrogel microstructures of arbitrary shape, set by the illumination pattern, and stiffness, set by the irradiation time and footprint of the objects. Columns are grafted on the PAM-coated plate and extend across the aqueous phase, up to the AN layer in contact with the oil phase. In Fig. 1 *C* and *D* we show schematically the process to create rigid hydrogel columns of arbitrary shape anywhere and at any time within a dynamic AN layer. As an example, here four adjacent rings are created, as seen in the fluorescence micrograph sequence in Fig. 1*E*. Notice that the fluorescent microtubules contained in the hydrogel volume are photobleached by the action of UV light, thus appearing dark in the fluorescence micrographs upon polymerization. In *SI Appendix*, Fig. S2, we demonstrate the system's capability of generating also soft columnar objects. In this case, a flexible ring that is continuously deformed by forces generated by the AN inside and outside the inclusion. Both rigid and flexible walls trigger the formation of active boundary layers (39) that determine the geometry of the enclosed AN. The high versatility of this protocol allows to print, either in sequence or simultaneously, both rigid and soft, deformable structures. This can be demonstrated by imprinting a combination of flexible pillars enclosed by a rigid ring; see Movie S3. This allows both to monitor the adaptation of the AN to a sudden change in boundary conditions, and to probe the local stresses exerted by the active material, as we discuss below.

In Situ Microrheology of the AN Layer. In this study, we take advantage of the elasticity of the soft hydrogel to imprint an array of compliant pillars with circular cross-section as microrheological probes for the AN layer (Fig. 2 *A*–*C*). Each pillar will act as a cantilever, anchored on the PAM-coated plate and bent by the action of the AN layer but also by the fluid phases that are set into motion by the AN layer: the oil phase, in contact with the free cylinder surface, and the aqueous phase, which will exert a drag force all along the hydrogel column (*SI Appendix*, section S1A). As we show in *SI Appendix*, section S1C, these effects can be neglected when compared to the force exerted by the AN layer, and will be ignored.

The AN layer exerts a combination of hydrodynamic, active, and elastic stresses that results in the so-called active turbulent regime (26, 32). Previous studies with this material suggested that hydrodynamic and active stresses have similar orders of magnitude, while elastic stresses are subdominant, except near topological defects (22, 40, 41). We will thus assume that column deflection is balanced by the effect of active and hydrodynamic (shear) stresses alone. This will lead to the determination of

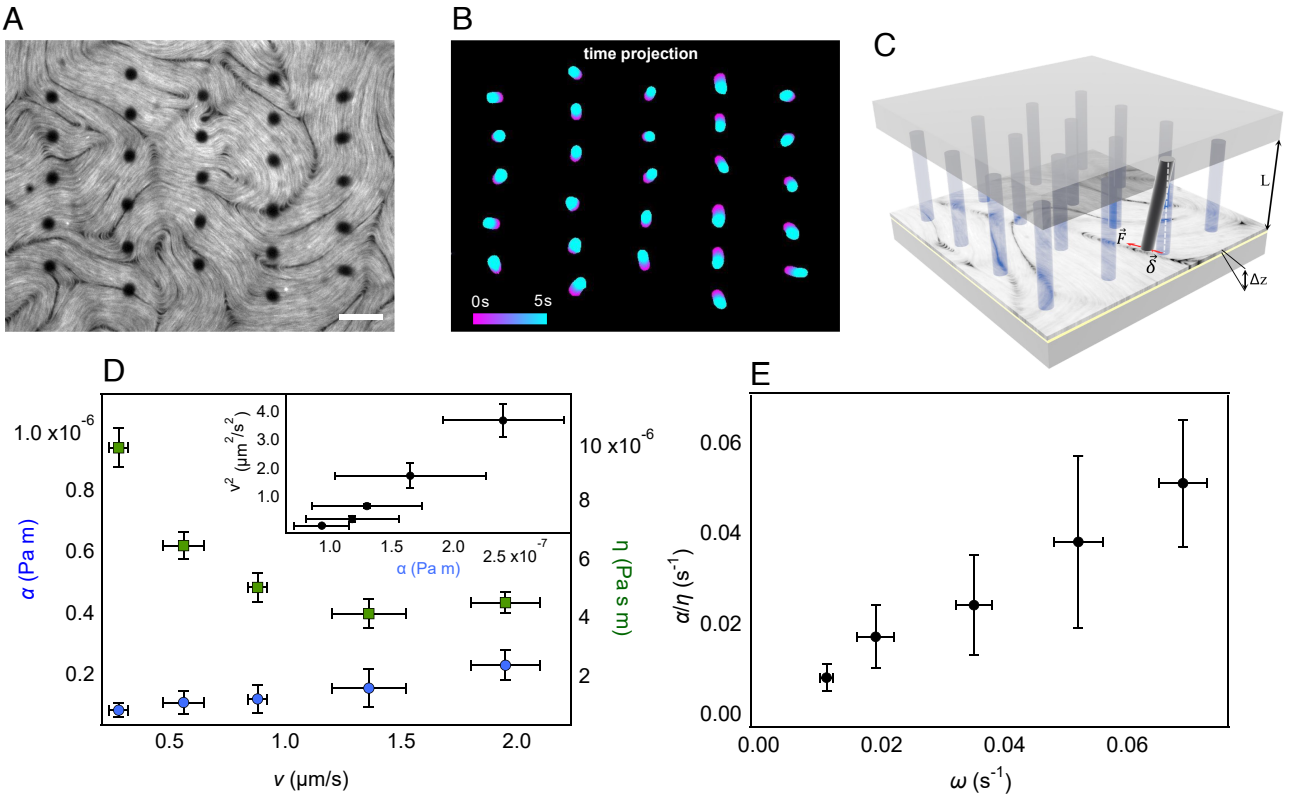

Fig. 2. Probing AN forces with elastic micro-pillars. (*A*) Fluorescence micrograph of an AN layer at the instant when a lattice of soft columns has been photo-polymerized (Movie S4). Irradiation time is 1.5 s. Scale bar is 50 μm. (*B*) Color-coded location of the columns' free surface during the first 5 s after polymerization. (*C*) The flexible columns are deflected by $\vec{\delta}$ due to the action of $\vec{F}$, the resultant of the viscous drag and active forces acting at the free end of each column, which are submerged a depth Δz in the AN layer. (*D*) Measured activity parameter and viscosity of the AN layer vs. the average speed of the AN flows. In the *Inset*, the square of the speed is plotted vs. the activity parameter. (*E*) Comparison between the inverse of the active time scale, α/η, computed from the parameters reported in panel (*D*), and the average vorticity, ω, obtained from the active flow velocity map. In (*D* and *E*), error bars are the SD of the mean for v and ω, CIs for the fitted parameters α and η, and the result of error propagation when required.

two important material parameters, the two-dimensional shear viscosity, η, and the two-dimensional activity parameter, α, of the AN layer, both assumed positive for our extensile material (22).

The force exerted by the AN is computed as,

$$F_i^{AN} = \iint_{S_{AN}} \sum_{j=1,2} \sigma_{ij}^{AN} n_j dS = \oint \sum_{j=1,2} \sigma_{ij}^{AN} n_j dl \; \Delta z$$
$$= \oint \sum_{j=1,2} \sigma_{ij}^{AN,2d} n_j dl, \qquad [1]$$

where σ_{ij}^{AN} is the stress in the AN, S_{AN} is the lateral cylindrical surface of thickness Δz that is submerged in the AN layer (Fig. 2*C*), n_j is the unit vector normal to the lateral surface, and the path integrals are performed along the circular edge of the cylinder free surface. The indices i, j refer to the in-plane spatial coordinates. Notice that this decomposition supposes to consider σ_{ij}^{AN} invariant across Δz. This further permits to define the two-dimensional AN stress tensor, $\sigma_{ij}^{AN,2d} = \sigma_{ij}^{AN} \Delta z$, with which we can implement the force balance without the need for a precise knowledge of the AN layer thickness.

The 2D stress tensor is further decomposed in terms of the dominant viscous and active stresses, $\sigma_{ij}^{AN,2d} = \sigma_{ij}^{vis} + \sigma_{ij}^{act}$, respectively defined as $\sigma_{ij}^{vis} = 2\eta\varepsilon_{ij}$, and $\sigma_{ij}^{act} = -\alpha Q_{ij}$, where, ε_{ij} denotes the strain rate tensor, and Q_{ij} is the traceless nematic tensor order parameter, both in their two-dimensional forms (22).

As the experimental determination of ε_{ij}, involving spatial velocity gradients, is prone to numerical artifacts, we have resorted to estimating the viscous drag force on each column using Lamb's equation (42), $F_i^{drag} = 4\pi\epsilon\eta^{3D} v_i \Delta z = 4\pi\epsilon\eta v_i$, where $\epsilon = [0.5 - \gamma - \ln(\frac{Re}{8})]^{-1}$ is the viscous drag coefficient (42). Notice that, as done before for σ_{ij}^{AN}, we transform 3d values of the viscosity of the AN layer into effective two-dimensional ones. Here, γ is Euler's constant and Re is the Reynolds number, which is in the range 2×10^{-9} to 6×10^{-8} in our experiments. This results in an average value $\epsilon = 0.052$, which we use in all our computations as it only varies within 5% in our range of Re values. Notice that we have defined the stress tensor neglecting pressure gradients and retaining only the viscous and active components. This is the usual approach in numerical studies (22) describing unbounded ANs. In the presence of obstacles, however, the evaluation of F_i^{drag} using Lamb's equation does include the effect of pressure gradients, which are, therefore, implicitly taken into account in our analysis.

For each hydrogel column, we write the force balance separating explicitly the distinctive linear contributions in η and α,

$$F_i^{def} = F_i^{drag} + F_i^{act} = F_i^{\eta}\eta + F_i^{\alpha}\alpha, \qquad [2]$$

with $F_i^{\eta} \equiv 4\pi\epsilon v_i$ and $F_i^{\alpha} \equiv -\oint \sum_{j=1,2} Q_{ij} n_j dl$.

This equation implies mechanical equilibrium between the active forces and cantilever flexion. Since the AN is intrinsically out of equilibrium, we will assume, as an approximation, that force balance is satisfied on each column right before it changes its initial bending direction or when it reaches a steady deflection value. Moreover, the velocity and orientational fields of the AN in the vicinity of each column, required to compute F_i^{η} and F_i^{α}, respectively, cannot be obtained with enough precision once columns are imprinted. For this reason, we will use the accurate measurement of these fields just before columns are polymerized.

The force required for the bending deflection of the cylindrical pillar is $F_i^{def} = \frac{3\delta_i EI}{L^3}$ (*SI Appendix*, section S1B), where δ_i denotes the in-plane component of the deflection, while E, I, and L correspond respectively to the Young's modulus (which we determine using fluids of known viscosity (*SI Appendix*, section S1D and Fig. S3), the second moment of inertia of the cylindrical column, and the height of the pillars, $L = 40$ μm (*Materials and Methods*). In our analysis, we have included columns of different radii in the range $r = 5.2$ μm to 9 μm, to achieve a deflection at mechanical equilibrium between r and $2r$ for all ATP concentrations. Our measurements show that the total force exerted on a single column is in the range 1 to 20 pN, depending on the column diameter and local fields of the AN. In all cases, we observe that the drag force due to active flows is typically 3 to 4 times larger than the corresponding force due to active stress. This is consistent with the experimental observation that, in general, pillars deflect along a direction close to that of the local active flows.

For each pillar, we write the force balance condition (Eq. **2**), which depends on α and η. We then fit the optimum values for α and η that more closely satisfy the force balance equations simultaneously for a set including dozens of pillars under the same experimental conditions. The results of our measurements are shown in Fig. 2*D*, where α and η are plotted as a function of the average speed of the active flow (49). The latter is used here as a reliable proxy for the system's activity. A calibration curve of speed vs. ATP concentration is presented in *SI Appendix*, Fig. S4*A*, which allows to plot α and η as a function of ATP concentration (*SI Appendix*, Fig. S4*B*). Our results show that α is around 2×10^{-7} Pa m, only weakly dependent on activity, while η is in the range $(4 \text{ to } 10) \times 10^{-6}$ Pa s m, revealing a shear thinning nature of the active material, as previously reported (43).

We have compared our direct measurement of η with an early strategy reported by Martínez-Prat et al. (26) based on a model for the kinetic energy spectra, and have found excellent agreement (*SI Appendix*, section S1F and Fig. S5). Moreover, earlier theoretical studies predicted a scaling relationship between the activity parameter and the average speed of the form $v^2 \sim \alpha$ (32), which we have validated with our experimental data (*Inset* in Fig. 2*D*). We have also verified that our measurements agree

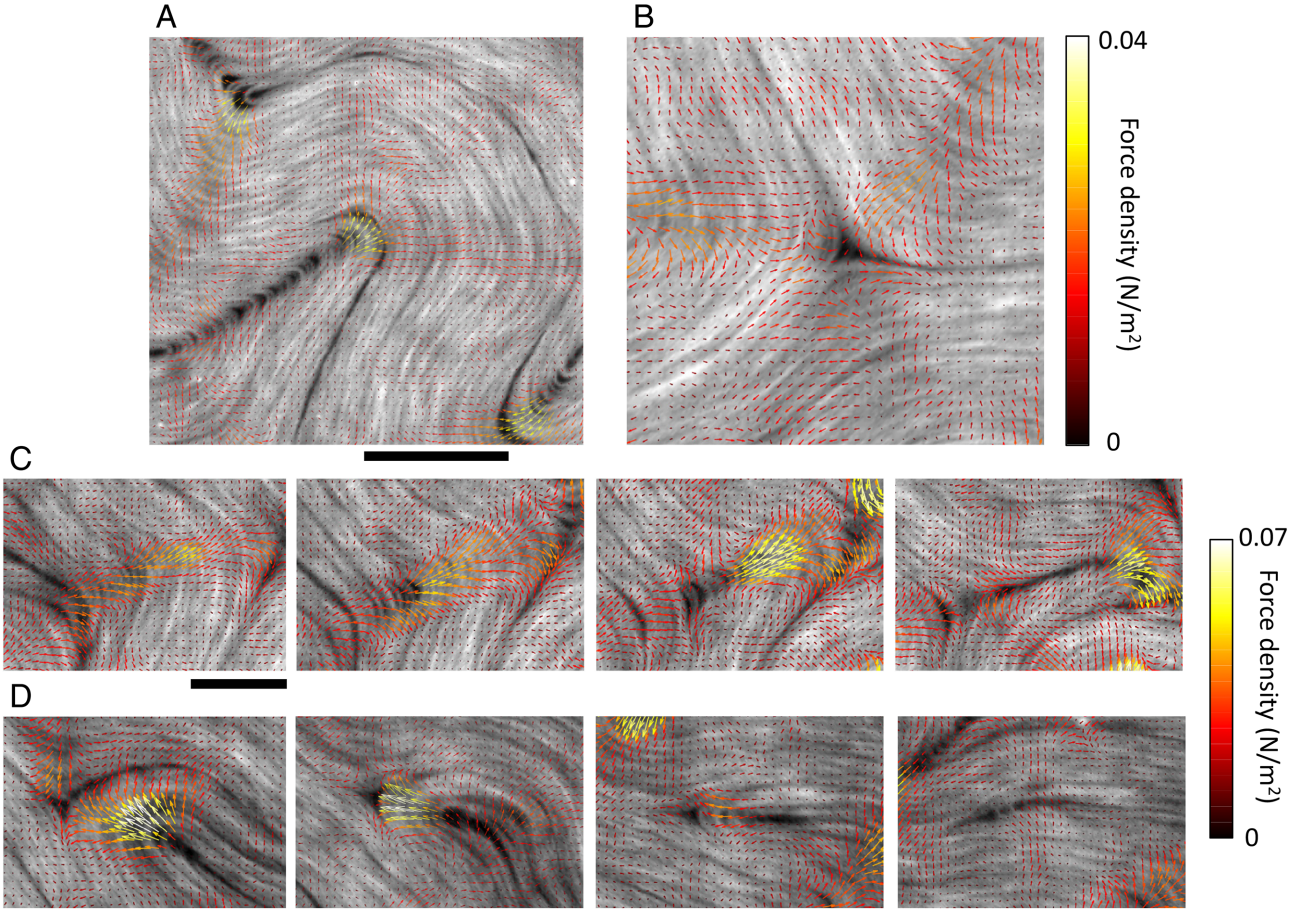

Fig. 3. Active nematic forces. (*A*) Force density map, obtained from $f_i = 2\eta\partial_j\epsilon_{ij} - \alpha\partial_j Q_{ij}$, in the vicinity of a $+1/2$ defect. The force density accumulates at the tip of the self-propelled defect. (*B*) In the vicinity of a $-1/2$ defect, the force density exhibits nearly three-fold symmetry. (*C*) Force density map during the unbinding of a defect pair. The force density accumulates at the tip of the bending filaments, leading to the formation of a $+1/2$ and $-1/2$ defect pair. Elapsed times from the first frame are 2, 8, and 12 s (Movie S5). (*D*) Force density map during the annihilation of a defect pair. The high force density at the tip of the moving $+1/2$ defect vanishes after coalescence. Elapsed times from the first frame are 9, 14, and 19 s (Movie S6). (Scale bars, 50 μm.)

with the theoretical expectation that α/η is related to the inverse of the intrinsic time scale of the AN, which we can extract from the average vorticity, ω. Indeed, Fig. 2*D* suggests that these two parameters are proportional, $\omega \sim \alpha/\eta$ (32, 40).

Having obtained reliable values for α and η at different activities, we can estimate a third material parameter, K, which encodes the bending rigidity of the active filaments. For this purpose, we resort to the scaling relation for the active length scale, $l_\alpha^2 \sim K/\alpha$ (22). In our experiments, we estimate $l_\alpha \sim n^{-1/2}$, where n is the average defect density, from which $K \sim \alpha/n$ can be estimated for each concentration of ATP (*SI Appendix*, Fig. S6). Our results suggest an average value $K \simeq 6\ 10^{-16}$N m, with a marginal increase with the concentration of ATP, indicating that microtubule bundling may be enhanced by ATP.

Having quantified the material parameters that determine the main local stress of the AN, the presented method enables us to quantitatively map, for any AN configuration, the resultant force density field, obtained as $f_i \simeq 2\eta\partial_j\epsilon_{ij} - \alpha\partial_j Q_{ij}$. Note that here we have also neglected the contribution from the AN elasticity, as discussed above. In Fig. 3 we apply this result to map the total force density field around a $+1/2$ (Fig. 3*A*) and a $-1/2$ (Fig. 3*B*) defect. The force patterns for each configuration, respectively parabolic and triangular, are consistent with previously reported theoretical results (22, 44). Experimental force patterns show that $+1/2$ defects self-propel from tail to head dragging the surrounding material. Conversely, we see that negative defects balance the local forces acting in their surroundings, leading to no net propulsion and exhibiting advected motion only (45, 46).

It is interesting to compare the relative strengths of the two dominant force contributions in the AN layer in the absence of obstacles. To this purpose, we have resolved the force density field into its active and viscous components near a $+1/2$ defect (*SI Appendix*, Fig. S7). The balance in this case is dominated by active forces, contrary to what was observed when computing the force balance for column deflection. In that case, viscous drag arising from no-slip boundary conditions on the hydrogel cylindrical surface resulted in strong forces in the direction of the average flow. Without obstacles, viscous force density is relatively weak and it opposes the self-propelling flows generated by the local active stress.

The propelling effect from accumulated internal stress within aligned microtubule bundles is best illustrated during the unbinding of defect pairs of opposite topological charge, one of the most distinctive events in the dynamics of the quasi-two-dimensional ANs. One of these events is illustrated in Fig. 3*C*, where the total force density increases at the tip of an unstable bending region. This promotes its growth, until a $+1/2$ defect unbinds, being self-propelled by a strong force density at its tip, while a $-1/2$ defect is left behind, surrounded by a stagnating force density field. The complementary scenario, namely that of defect annihilation, is shown in Fig. 3*D*. The $+1/2$ defect is propelled by a strong force field acting on its tip toward a nearly stationary $-1/2$ defect. Recombination leads to a locally defect-free region where the force field vanishes.

The versatility of the employed method allows us to polymerize a combination of rigid and compliant inclusions. This opens the door to measuring the force fields generated in confined AN arrangements. Some examples are presented in Fig. 4. Fig. 4 *A* and *B* include a system of two rotating positive defects created after active flows adapt to sudden ring confinement. Stresses are probed with one compliant column centered in one case, and off-center in the other. Column bending in each situation clearly reflects the stress pattern created by the AN, with small deformations near the center (*Top*) and large deformations in the off-centered case (*Bottom*). Fig. 4 *C* and *D* explore, in a similar fashion, a $-1/2$ defect captured within a rigid ring. Here, the AN is prone to destabilization under confinement. An array of five compliant pillars seeded in a centered-square arrangement exhibit an inappreciable deformation of the central probe and small, albeit measurable, deformations of the outer columns that indicate a torque pattern.

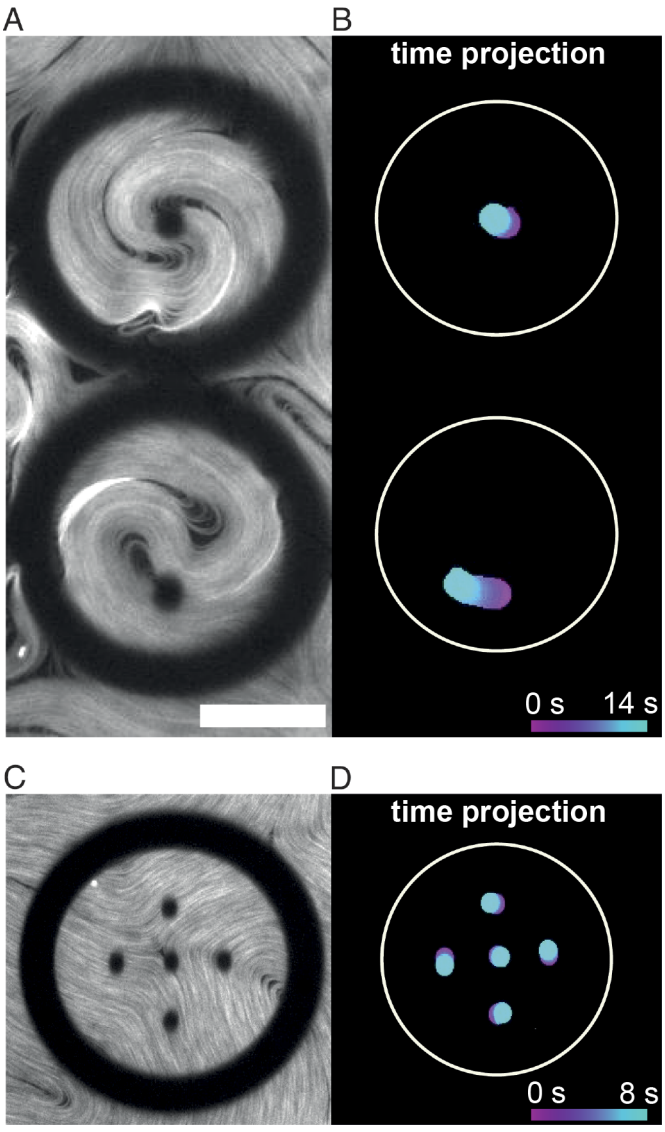

Fig. 4. Mixed rigid and compliant objects for probing forces in confined AN arrangements. (*A*) Two wide rings impose rigid confinement on the AN layer, leading to the reorganization of the active flow into a pair of rotating $+1/2$ defects. Once the flow is steady, we imprint additional compliant columns, either at the *Center* (*Top* panel) or off-centered (*Bottom* panel) with respect to the rigid ring (Movie S7). (*B*) Compliant columns deformation during the first 14 s after printing. (*C*) A rigid ring and a set of flexible columns are simultaneously imprinted around a $-1/2$ defect using 1.5 s of irradiation (Movie S8). (*D*) Column deformation during the first 8 s after printing. The (scale bar is 50 μm.)

Final Remarks and Conclusions

Synthetic active biomaterials, like those composed of protein filaments and motors, have been used as models for complex living systems. Theories to characterize these materials rely on a few parameters whose measurement is challenging. The demonstrated method of in situ photopolymerization of compliant

cantilevers enables direct precise measurement of the activity, shear viscosity, and, indirectly, an elastic constant. Our approach involves important simplifying assumptions, such as ignoring the distortion caused by the sudden appearance of solid columns on the velocity and orientational fields or ignoring the influence of elastic stresses in the active material. As a result, regions with high defect density or with very uniformly aligned active filaments cannot be probed with this method. Nevertheless, the possibility to perform an assessment based on a large number of probes allows to obtain the relevant parameters with statistically meaningful values.

The reported strategy of hybridizing the microtubule/kinesin system with a photopolymerizable monomer not only deepens significantly our understanding of the constitutive characteristics of this active gel but opens side by side endless possibilities to control the active nature of this particular and other similar materials. The incorporation of active materials with externally tunable characteristics into microchips represents a significant step forward in the design of future micro-machines built on the principles of active matter.

Materials and Methods

Polymerization of Microtubules. Microtubules ($\sim$ 1 μm) were polymerized from heterodimeric (α,β)-tubulin from bovine brain (Brandeis University Biological Materials Facility). Tubulin was incubated at 37 °C for 30 min in aqueous M2B buffer (80 mM Pipes (piperazine-N,N′-bis(2-ethanesulfonic acid)), 1 mM EGTA (ethylene glycol-bis(β-aminoethyl ether)-N,N,N′,N′-tetraacetic acid), 2mM $MgCl_2$) (Sigma; P1851, E3889 and M4880, respectively) prepared with Milli-Q water and supplemented with the antioxidant agent dithiothreitol (DTT) (Sigma 43815) and nonhydrolyzable guanosine triphosphate (GTP) analog GMPCPP (guanosine-5′-[(α,β)-methyleno]triphosphate) (Jena Biosciences, NU-405) up to a concentration of 1 mM and 0.6 mM, respectively. To allow the observation under fluorescence microscopy, 3% of the total tubulin concentration (8 mg ml^{-1}) was labeled with Alexa 647. Afterward, the mixture was annealed at room temperature for 4 h and kept at −80 °C until use.

Kinesin Expression. The kinesin used in the experiments was the heavy-chain kinesin-1 from *Drosophila melanogaster* truncated at residue 401, fused to biotin carboxyl carrier protein (BCCP), and labeled with six histidine tags (K401-BCCP-6His). This was expressed in *Escherichia coli* using the plasmid WC2 from the Gelles Laboratory (Brandeis University) and purified with a nickel column. After dialysis against 500 mM imidazole aqueous buffer, kinesin concentration was estimated by means of absorption spectroscopy. Finally, the kinesin was stored in a 40% (wt/vol) aqueous sucrose solution at −80 °C until use.

Assembly of the Microtubule-Based Active Mixture. Biotinylated kinesin motor proteins were incubated on ice for 30 min with tetrameric streptavidin (Invitrogen; 43-4301) at the specific ratio of 2:1 to obtain kinesin-streptavidin motor clusters. The standard preparation of the active mixture consisted of a M2B aqueous solution that contains ATP (adenosine 5′-triphosphate) (Sigma; A2383), the motor clusters, microtubules, and the depleting agent PEG (poly(ethylene glycol)) (20 kDa, Sigma;95172). To maintain a constant concentration of ATP during the experiments, an enzymatic ATP-regeneration system was added, consisting of phosphoenolpyruvate (PEP) (Sigma; P7127) that fueled the enzyme pyruvate kinase/lactate dehydrogenase (PKLDH) (Sigma; P0294) to convert ADP (adenosine 5′-diphosphate) back to ATP. The mixture also contained several antioxidants to avoid photobleaching during the fluorescence imaging: DTT, glucose oxidase (Sigma; GT141), catalase (Sigma; C40), Trolox (6-hydroxy-2,5,7,8-tetramethylchroman-2-carboxylic acid) (Sigma; 238813), and glucose (Sigma; G7021). The constituents of the photopolymerizing hydrogel were incorporated in solid form to the active mixture. The former consisted of the photoinitiator lithium phenyl-2,4,6-trimethylbenzoylphosphinate (LAP, TCI; L0290) and the monomer 4-Arm PEG-Acrylate 5 kDa (4PEG5k, Biochempeg; A44009-5k). The final concentrations of each reagent used in the preparation of the active material are shown in Table 1.

Table 1. Composition of all solutions (including buffer used for their preparation), and concentration of the different species in the final mixture

Compound	Buffer	Final Conc.	Units
PEG (20 kDa)	M2B	1.54	% w/v
PEP	M2B	25.68	mM
$MgCl_2$	M2B	3.12	mM
ATP	M2B	60 to 296	μM
DTT	M2B	5.21	mM
Streptavidin	M2B	0.01	mg/mL
Trolox	Phosphate	1.93	mM
Catalase	Phosphate	0.04	mg/mL
Glucose	Phosphate	3.20	mg/mL
Glucose Oxidase	Phosphate	0.21	mg/mL
PK	Original	25.01	u/mL
LDH	Original	24.91	u/mL
Kinesin	Original	0.08	mg/mL
Microtubules	Original	1.85	mg/mL
LAP	Mixture	0.226	% w/v
4PEG5k	Mixture	4.52	% w/v

Acronyms used in this table are PEG (poly-ethylene glycol); PEP (phosphoenol pyruvate); ATP (adenosine triphosphate); PK (pyruvate kinase); LDH (lactic dehydrogenase); DTT (1,4-dithiothreitol); 4PEG5k (4-Arm PEG-Acrylate 5 kDa); and LAP (lithium phenyl-2,4,6-trimethylbenzoylphosphinate). The two latter compounds where directly incorporated to the active mixture. M2B buffer: 80 mM PIPES (piperazine-N,N′-bis(2-ethanesulfonic acid)) pH 6.8, 2 mM $MgCl_2$ 1 mM EGTA (egtazic acid). Phosphate buffer: 20 mM Phosphate buffer (6.68 mM KH_2PO_4, 12.32 mM K_2HPO_4) pH 7.2; Original: species is obtained already dissolved in its custom buffer.

Active Nematic Cell. The experiments were carried out using flow cells with a channel of 3 to 5 mm width and 50 μm height. The cell was composed of a bioinert and superhydrophilic polyacrylamide-coated glass and a hydrophobic Aquapel-coated glass, separated using a 50 μm thick double-sided tape. The cell was first filled by capillarity with fluorinated oil (HFE7500; Fluorochem 051243) which contains 2% of a fluorosurfactant copolymer (RanBiotechnologies, 008 Fluorosurfactant). The active material was subsequently introduced in the cell by capillarity. To avoid evaporation, the cell was sealed using petroleum jelly. This preparation resulted in the approximate thickness for each phase (as determined using fluorescence confocal microscopy): 10 μm for the oil layer, 5 to 10 μm for the AN layer, and 30 to 35 μm for the aqueous subphase.

Observation of the Active Nematic. The observation of the active nematic layer was carried out by means of fluorescence microscopy. We used a Nikon Eclipse Ti2-e equipped with a white LED source (Thorlabs MWWHLP1) and a Cy5 filter cube (Edmund Optics). Images were captured using an ExiBlue CCD camera (QImaging) operated with the open-source software ImageJ μ-Manager.

Hydrogel Polymerization. The fluorescence microscope was modified in order to incorporate a digital micromirror device (DMD) UV light projector (Texas Instruments LightCrafter 4500, with a 2W 385 nm LED; EKB Technologies, Ltd.), see *SI Appendix*, Fig. S1. Projected patterns are incorporated into the light path of the inverted microscope by means of a collimating lens (f = +150 mm) and a 505 nm dichroic mirror (Thorlabs DMLP505R), and are focused on the sample by means of the microscope objectives, reaching a lateral resolution up to a few microns. The DMD projector is connected as an external monitor to a computer, thus enabling real time control of the projected patterns using MS-PowerPoint slides. For the experiments shown in this work, the hydrogel was polymerized using an x20 objective, resulting in a light power density of 3.1 W cm^{-2}. The resulting columns have a height of 40 μm, of which 5 to 10 μm are embedded in the AN layer.

The rigidity of the hydrogel structures can be adjusted by a combination of the irradiation time and the power of the LED light source that feeds the DMD. Since

the AN features self-sustained flows that drag the water subphase, polymerization must be performed quickly to prevent the formation of distorted shapes, as the incipient hydrogel is advected by the active flows. In practice, we require that the maximum flow advection during polymerization is under 2 $\mu m\ s^{-1}$, which limits ATP concentration to be below 450 μM. With the used concentration of monomer and initiator, we find that the polymerization time must be in the range 750 to 1250 ms for soft and 1,500 to 3,000 ms for rigid structures. As an alternative to adjusting the polymerization time, the lateral compliance of the structures can be set by controlling their in-plane cross-section.

Sample Characterization. The director field of the active nematic layer was obtained using a coherence-enhanced diffusion filtering (CEDF) MatLab code (47) applied on fluorescence images. Tracer-free velocimetry analysis of the active nematic was performed with the public MatLab App PIVlab. This approach is reliable as long as microscopy observations are restricted to 20x objectives or less (48). Higher magnifications or increased precision would require the use of tracer particles or sparse fluorescent microtubules and a two-channel fluorescence observation.

Further analysis of director and velocity field data was performed with custom-written MatLab scripts. When required, PIV data was linearly interpolated to match the grid of the director field.

Young's Modulus Determination. The hydrogel Young's modulus was determined in situ, in a flow cell prepared as explained above, filled by capillarity with the buffer solution and gellifying agents but without motor proteins and microtubules. Cylindrical columns were polymerized using the protocol described above and were deformed by flowing liquids of known viscosity by capillarity. We used methylcellulose (Sigma; M0512) solutions of concentrations between 0.18 and 0.54% (w/vol) prepared in M2B buffer. Their viscosity was measured using a Brookfield Ametek DVE Viscosimeter with a Yula-15 spindle. To measure the average flow speed, a 5% (vol/vol) concentration of fluorescent particles of diameter 1 μm (Bangs Laboratories; FCDG006) were incorporated into the solution, and average speeds where determined by tracking individual particles using ImageJ.

Data, Materials, and Software Availability. Experimental image sequences and measured forces required for the force balances are freely available in https://doi.org/10.17605/OSF.IO/CAQF2 (49).

ACKNOWLEDGMENTS. We are indebted to the Brandeis University MRSEC Biosynthesis facility for providing the tubulin. We thank M. Pons, A. LeRoux, and G. Iruela (Universitat de Barcelona) for their assistance in the expression of motor proteins. I.V.-C. acknowledges funding from Generalitat de Catalunya through a FI-2020 PhD. Fellowship. P.G. acknowledges support from Generalitat de Catalunya through the Beatriu de Pinós program (grant number 2020 BP 00248). I.V.-C., J.I.-M., and F.S. acknowledge funding from MICINN/AEI/10.13039/501100011033 (Grants No. PID2019-108842GB-C22 and PID2022-137713NB-C21). Brandeis University MRSEC Biosynthesis facility is supported by NSF MRSEC 2011846. We acknowledge helpful discussions with C.S.-M. and N.I.-M.

Author affiliations: [a]Department of Materials Science and Physical Chemistry, Universitat de Barcelona, Barcelona 08028, Spain; [b]Institute of Nanoscience and Nanotechnology, IN2UB, Universitat de Barcelona, Barcelona 08028, Spain; and [c]Institute for Bioengineering of Catalonia, The Barcelona Institute for Science and Technology, Barcelona 08028, Spain

1. F. Sagués, *Colloidal Active Matter: Concepts, Experimental Realizations, and Models* (Taylor & Francis, London, ed. 1, 2023).
2. S. Ramaswamy, The mechanics and statistics of active matter. *Annu. Rev. Condens. Matter Phys.* **1**, 323–345 (2010).
3. M. C. Marchetti *et al*., Hydrodynamics of soft active matter. *Rev. Mod. Phys.* **85**, 1143–1189 (2013).
4. J. E. Herbert-Read *et al*., Inferring the rules of interaction of shoaling fish. *Proc. Natl. Acad. Sci. U.S.A.* **108**, 18726–18731 (2011).
5. W. Bialek *et al*., Statistical mechanics for natural flocks of birds. *Proc. Natl. Acad. Sci. U.S.A.* **109**, 4786–4791 (2012).
6. J. Buhl *et al*., From disorder to order in marching locusts. *Science* **312**, 1402–1406 (2006).
7. T. B. Saw *et al*., Topological defects in epithelia govern cell death and extrusion. *Nature* **544**, 212–216 (2017).
8. K. Kawaguchi, R. Kageyama, M. Sano, Topological defects control collective dynamics in neural progenitor cell cultures. *Nature* **545**, 327–331 (2017).
9. C. Blanch-Mercader *et al*., Turbulent dynamics of epithelial cell cultures. *Phys. Rev. Lett.* **120**, 208101 (2018).
10. G. Duclos *et al*., Spontaneous shear flow in confined cellular nematics. *Nat. Phys.* **14**, 728 (2018).
11. I. Theurkauff, C. Cottin-Bizonne, J. Palacci, C. Ybert, L. Bocquet, Dynamic clustering in active colloidal suspensions with chemical signaling. *Phys. Rev. Lett.* **108**, 268303 (2012).
12. J. Palacci, S. Sacanna, A. P. Steinberg, D. J. Pine, P. M. Chaikin, Living crystals of light-activated colloidal surfers. *Science* **339**, 936–939 (2013).
13. I. Buttinoni *et al*., Dynamical clustering and phase separation in suspensions of self-propelled colloidal particles. *Phys. Rev. Lett.* **110**, 238301 (2013).
14. W. Wang, W. Duan, S. Ahmed, A. Sen, T. E. Mallouk, From one to many: Dynamic assembly and collective behavior of self-propelled colloidal motors. *Account. Chem. Res.* **48**, 1938–1946 (2015).
15. H. P. Zhang, A. Be'er, E. L. Florin, H. L. Swinney, Collective motion and density fluctuations in bacterial colonies. *Proc. Natl. Acad. Sci. U.S.A.* **107**, 13626–13630 (2010).
16. H. H. Wensink *et al*., Meso-scale turbulence in living fluids. *Proc. Natl. Acad. Sci. U.S.A.* **109**, 14308–14313 (2012).
17. H. Li *et al*., Data-driven quantitative modeling of bacterial active nematics. *Proc. Natl. Acad. Sci. U.S.A.* **116**, 777–785 (2019).
18. T. Turiv *et al*., Polar jets of swimming bacteria condensed by a patterned liquid crystal. *Nat. Phys.* **16**, 481–487 (2020).
19. T. Sanchez, D. T. Chen, S. J. DeCamp, M. Heymann, Z. Dogic, Spontaneous motion in hierarchically assembled active matter. *Nature* **491**, 431–434 (2012).
20. B. Martínez-Prat, J. Ignés-Mullol, J. Casademunt, F. Sagués, Selection mechanism at the onset of active turbulence. *Nat. Phys.* **15**, 362 (2019).
21. D. Needleman, Z. Dogic, Active matter at the interface between materials science and cell biology. *Nat. Rev. Mat.* **2**, 17048 (2017).
22. A. Doostmohammadi, J. Ignés-Mullol, J. M. Yeomans, F. Sagués, Active nematics. *Nat. Commun.* **9**, 3246 (2018).
23. R. Zhang *et al*., Spatiotemporal control of liquid crystal structure and dynamics through activity patterning. *Nat. Mater.* **20**, 875–882 (2021).
24. P. Guillamat, J. Ignés-Mullol, S. Shankar, M. C. Marchetti, F. Sagués, Probing the shear viscosity of an active nematic film. *Phys. Rev. E* **94**, 060602 (2016).
25. A. J. Tan *et al*., Topological chaos in active nematics. *Nat. Phys.* **15**, 1033–1039 (2019).
26. B. Martínez-Prat *et al*., Scaling regimes of active turbulence with external dissipation. *Phys. Rev.* **X 11**, 031065(1–16) (2021).
27. P. Guillamat, J. Ignés-Mullol, F. Sagués, Control of active liquid crystals with a magnetic field. *Proc. Natl. Acad. Sci. U.S.A.* **113**, 5498–502 (2016).
28. P. Guillamat, J. Ignés-Mullol, F. Sagués, Taming active turbulence with patterned soft interfaces. *Nat. Commun.* **8**, 564 (2017).
29. F. C. Keber *et al*., Topology and dynamics of active nematic vesicles. *Science* **345**, 1135–1139 (2014).
30. K. T. Wu *et al*., Transition from turbulent to coherent flows in confined three-dimensional active fluids. *Science* **355**, eaal1979 (2017).
31. J. Hardoüin *et al*., Reconfigurable flows and defect landscape of confined active nematics. *Commun. Phys.* **2**, 121 (2019).
32. L. Giomi, Geometry and topology of turbulence in active nematics. *Phys. Rev. X* **5**, 031003 (2015).
33. R. Zhang, Y. Zhou, M. Rahimi, J. J. De Pablo, Dynamic structure of active nematic shells. *Nat. Commun.* **7**, 13483 (2016).
34. R. Alert, J. F. Joanny, J. Casademunt, Universal scaling of active nematic turbulence. *Nat. Phys.* **16**, 682–688 (2020).
35. D. J. G. Pearce, P. W. Ellis, A. Fernandez-Nieves, L. Giomi, Geometrical control of active turbulence in curved topographies. *Phys. Rev. Lett.* **122**, 168002 (2019).
36. K. Thijssen *et al*., Submersed micropatterned structures control active nematic flow, topology, and concentration. *Proc. Natl. Acad. Sci. U.S.A.* **118**, 1–10 (2021).
37. P. Guillamat, C. Blanch-Mercader, G. Pernollet, K. Kruse, A. Roux, Integer topological defects organize stresses driving tissue morphogenesis. *Nat. Mater.* **21**, 588–597 (2022).
38. B. D. Fairbanks, M. P. Schwartz, C. N. Bowman, K. S. Anseth, Photoinitiated polymerization of peg-diacrylate with lithium phenyl-2,4,6-trimethylbenzoylphosphinate: polymerization rate and cytocompatibility. *Biomaterials* **30**, 6702–6707 (2009).
39. J. Hardoüin *et al*., Active boundary layers in confined active nematics. *Nat. Commun.* **13**, 6675 (2022).
40. C. Joshi *et al*., Data-driven discovery of active nematic hydrodynamics. *Phys. Rev. Lett.* **129**, 258001 (2022).
41. M. Golden, R. O. Grigoriev, J. Nambisan, A. Fernandez-Nieves, Physically informed data-driven modeling of active nematics. *Sci. Adv.* **9**, eabq6120 (2023).
42. L. D. Landau, L. E. M., *Fluid Mechanics* (Pergamon Press, Oxford, ed. 2, 1987).
43. D. P. Rivas, T. N. Shendruk, R. R. Henry, D. H. Reich, R. L. Leheny, Driven topological transitions in active nematic films. *Soft Matter* **16**, 9331–9338 (2020).
44. M. Serra, L. Lemma, L. Giomi, Z. Dogic, L. Mahadevan, Defect-mediated dynamics of coherent structures in active nematics. *Nat. Phys.* **19**, 1355–1361 (2023).
45. L. Giomi, M. J. Bowick, X. Ma, M. C. Marchetti, Defect annihilation and proliferation in active nematics. *Phys. Rev. Lett.* **110**, 228101 (2013).
46. L. Giomi, M. J. Bowick, P. Mishra, R. Sknepnek, M. Cristina Marchetti, Defect dynamics in active nematics. *Philos. Trans. A Math Phys. Eng. Sci.* **372**, 20130365 (2014).
47. P. W. Ellis, J. Nambisan, A. Fernandez-Nieves, Coherence-enhanced diffusion filtering applied to partially-ordered fluids. *Mol. Phys.* **118**, e1725167 (2020).
48. A. M. Tayar, L. M. Lemma, Z. Dogic, Assembling microtubule-based active matter. *Methods Mol. Biol.* **2430**, 151–183 (2022).
49. I. Vélez-Cerón, P. Guillamat, F. Sagués, J. Ignés-Mullol, AN microrheology. OSF. https://doi.org/10.17605/OSF.IO/CAQF2. Deposited 6 October 2023.